ChemComm

COMMUNICATION

View Article Online
View Journal

Cite this: DOI: 10.1039/d5cc00460h

Received 28th January 2025,
Accepted 7th July 2025

DOI: 10.1039/d5cc00460h

rsc.li/chemcomm

Bismuth/tin-based artificial interface for overcoming the anode passivation of rechargeable magnesium batteries†

Xiaolong Hou,[a] Jingfei Guan,[a] Baifei Wu,[b] Caini Yi,[a] Shuo Wang,[a] Guimiao Wang,[a] Hang Yang,[a] Min Liu,[a] Meilin Chen,[a] Danmei Yu, *[a] Liyong Gan [b] and Xiaoyuan Zhou *[b]

A bimetallic Bi/Sn artificial interface layer is constructed on an Mg anode *via* displacement reaction to address passivation challenges in ether-based electrolytes. Compared to the nucleation overpotential of Mg (−3.21 V), that of the fabricated BiSn@Mg is lower (0.098 V), and its deposition overpotential is below 0.21 V. The BiSn@Mg//BiSn@Mg cell can run stably for 4000 h with a good rate capability. The constructed artificial interface enhances Mg/electrolyte compatibility and reaction kinetics. This work advances reversible Mg plating/stripping in ether-based electrolytes.

Recently, the surging demand for portable electronic devices and electric vehicles has driven significant progress in the energy storage field.[1,2] Rechargeable magnesium batteries (RMBs) are emerging as formidable alternatives to lithium-ion batteries (LIBs) owing to their several advantages: first, magnesium (Mg) has a superior theoretical specific capacity (3833 mA h cm^{-3}),[3–5] which is particularly favorable for energy storage devices with limited storage space;[6,7] second, the Mg metal anode (MMA) exhibits a rather low redox potential (−2.37 V *vs.* SHE), so RMBs can provide a higher working voltage; and third, Mg shows high terrestrial abundance and safety compared with lithium metal. However, the practical application of RMBs is strictly hindered due to several challenges regarding MMA performance. On the one hand, the uneven deposition of magnesium ions during operation of RMBs under high current densities may lead to piercing of the separator due to dendrite formation and generation of internal short circuits, which poses safety hazards and results in rapid degradation of battery performances. On the other hand, passivation layers easily form on the metal anode in RMBs because magnesium, due to its strong reducibility,triggers a series of side reactions with traditional $Mg(TFSI)_2$/DME electrolytes.[8,9] Consequently, insulating components such as MgO and $Mg(OH)_2$ can gradually form on the MMA surface during charge–discharge processes, and these formations seriously hinder the diffusion of Mg ions and the electrode reaction kinetics. This hindrance occurs because the passivation layer on the MMA substantially obstructs the reversible plating/stripping of Mg, while the solid electrolyte interface (SEI) coating on the anode in LIBs can facilitate transport of lithium ions.[8–10] Therefore, operation of RMBs is marked by a short cycle life with emerging high polarization and poor stability.[11–15]

Alleviating the passivation of the MMA in conventional ether-based electrolytes is the key to improving the cycling reversibility and stability of Mg plating/stripping on the anode of an RMB.[16–18] Numerous studies have been dedicated to the development of an artificial SEI on the Mg electrode surface, which has shown significant potential in improving Mg^{2+} migration kinetics and inhibiting deleterious reactions with electrolyte.[19–24] Luo *et al.*[25] created an *in situ* protective layer by introducing $GeCl_4$ into an ether-based electrolyte to inhibit passivation on the MMA. However, this approach comes with some issues, such as chloride-induced corrosion of the cell components and the unpredictable nature of the chemical reactions. These issues could seriously hinder the effective formation of a stable SEI layer, thus lowering the cycling stability. To tackle these challenges, the subsequent research shifted its focus from directly incorporating chlorides into the electrolyte to facilitating their *in situ* formation or preparing an artificial interface layer on the Mg electrode beforehand, thereby effectively mitigating the corrosive effects of chloride ions. A Sn-based artificial SEI composed of Mg_2Sn alloy prepared by Luo *et al.*[26] through an *ex situ* soaking process effected a facilitated and rapid ion transport, while the insulating composition $MgCl_2/SnCl_2$ in the modified layer provided the essential gradient of potential to prevent surface deposition. Such strategies align with interfacial engineering principles used for stabilizing nanostructured carriers.[27,28] Furthermore, Pan *et al.*[29] successfully developed an In/$MgCl_2$/Mg SEI layer through a hydrolysis approach and introduced the concept of relative compactness

[a] School of Chemistry and Chemical Engineering, Chongqing University, Chongqing 401331, P. R. China. E-mail: yudanmei-1@163.com
[b] College of Physics, Chongqing University, Chongqing, 401331, P. R. China. E-mail: xiaoyuan2013@cqu.edu.cn

† Electronic supplementary information (ESI) available. See DOI: https://doi.org/10.1039/d5cc00460h

density, which offers a method for evaluating the density and chemical reactivity of the artificial SEI layer. Sustainable approaches, like those using eco-friendly materials,[30] highlight scalable solutions for low-cost SEI layers. Nevertheless, the single-component SEI layer presents some limitations, including suboptimal electrical contact activity and magnesiumphilicity among the constituent elements. Consequently, the overpotential of an MMA tends to increase progressively during the charge–discharge process. It is important to design and develop a simple, low-cost SEI layer to resolve present problems, which is essential for improving the cycling reversibility and stability of plating/stripping on MMAs.[31]

Herein, we have proposed a strategy for fabricating a BiSn artificial interface layer by carrying out a replacement reaction between Mg and two-component metal salts. Including this artificial interface effectively lowers the energy barriers to the adsorption and diffusion of Mg, enhances the affinity to anode-electrolyte interface and electrode reaction kinetics, thus creating a BiSn@Mg anode showing electrochemical performance markedly better than that of pristine Mg. Therefore, BiSn@Mg//BiSn@Mg exhibits a very low overpotential and exceptional cycling stability and can operate stably and continuously for over 4000 h at 0.01 mA cm^{-2} and maintain an overpotential below 0.2 V. Furthermore, the results of experiments with BiSn@Mg//Mo_6S_8 also demonstrate that the artificial interface layer effectively mitigates the interfacial reaction of electrode with electrolyte, enabling rapid and reversible plating/stripping of Mg.

SEM images in Fig. 1(a) and (b) clearly show the artificial interface layer to be composed of many spherical particles with dimensions of several microns and forming with a thickness of about 15 μm on the Mg surface. The formation of the artificial interface layer can be also observed from the optical photographs in the inset of Fig. 1(a). An EDS mapping of the cross-section of the BiSn@Mg in Fig. 1(c–f) shows Bi and Sn elements distribute mainly in artificial interface layer, and Mg element predominantly under its ''bottom'' while Cl from reaction residue. This result confirms that the artificial interface layer is mainly composed of Bi and Sn elements. Moreover, the thickness, crystal structure and elemental distribution of this artificial interface layer are almost unchanged over the course of 4000 h of charge–discharge, as evidenced by the results shown in Fig. S1 and S2 (ESI†), suggesting excellent structural stability. The SEM images and element mappings acquired of Sn@Mg and Bi@Mg are provided in Fig. S3 and S4 (ESI†), and suggest significant differences between them and BiSn@Mg. They also indicate that the artificial interface can be fabricated on an Mg surface by carrying out a simple displacement reaction. The spherical particles are also observed in an HR-TEM image, shown in Fig. 1(g), while the (101) plane of Bi with a lattice spacing of 3.28 Å and the (211) plane of Sn with a lattice spacing of 2.01 Å are seen in the acquired lattice fringe images, shown in Fig. 1(h–j). The artificial interface formed on the Mg surface is further confirmed to be mainly composed of Sn and Bi. Moreover, the interface contact between Bi and Sn could result in the formation of heterogeneous interfaces, which are conducive to enhancing the adsorption and diffusion of Mg^{2+} through synergistic interactions.[32]

Characteristic peaks of Mg (PDF#35-0821), Bi (PDF#44-1246), and Sn (PDF#04-0673) are seen in the XRD pattern acquired of a produced BiSn@Mg shown in Fig. 2(a), implying that the BiSn@Mg consists of metallic Mg, Sn and Bi. The XRD pattern confirms the crystalline nature of BiSn@Mg, despite its synthesis *via* displacement reaction between Mg and $BiCl_3$/$SnCl_2$. The XRD pattern of pristine Mg, provided in Fig. 2(b), only shows the characteristic peaks of Mg, in accordance with the Mg metal (PDF#35-0821). The XRD patterns acquired of Sn@Mg and Sn@Mg are also provided, in Fig. S5 (ESI†). The Bi 4f region of the XPS spectrum acquired of BiSn@Mg is provided in Fig. 2(c), and shows peaks located at 156.9 eV ($4f_{7/2}$) and 162.5 eV ($4f_{5/2}$), corresponding to Bi^0 species, and peaks at 159.7 eV ($4f_{7/2}$) and 165.1 eV ($4f_{5/2}$), attributed to Bi^{3+} species.[33] The presence of Bi^{3+} can be owed to trace residues of reactant and the bismuth oxidation due to the inevitable exposure of samples in air during the XPS test process shown in Fig. S13 (ESI†).[34] The Mg 1s region of the spectrum of BiSn@Mg, provided in Fig. 2(d), shows three separate peaks, at binding

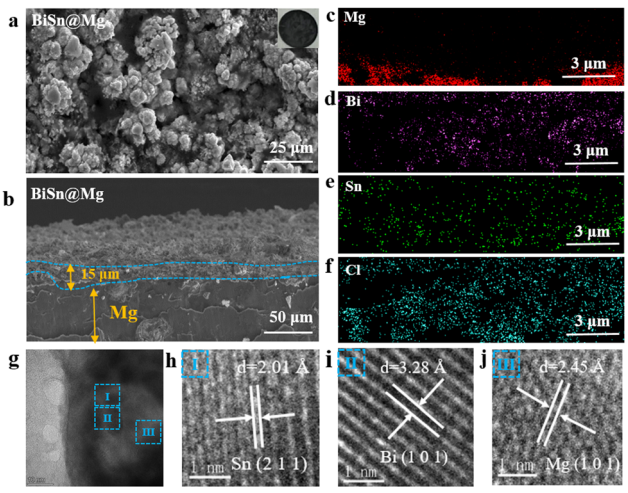

Fig. 1 (a) Top-view SEM image and optical photograph (inset), and (b) cross-sectional view SEM image of BiSn@Mg. (c)–(f) EDS mapping images of different elements in interface layer. (g) HR-TEM images of interface layer. (h)–(j) Lattice fringe images of regions I, II and III in panel (g).

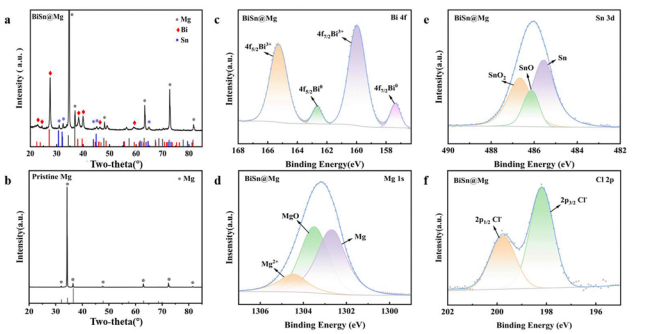

Fig. 2 (a) and (b) XRD patterns of (a) BiSn@Mg and (b) pristine Mg. (c) Bi 4f, (d) Mg 1s, (e) Sn 3d and (f) Cl 2p regions at high resolution of the XPS spectrum of BiSn@Mg.

energies of 1302.8 eV, 1303.8 eV, and 1304.5 eV, confirming the presence of Mg, MgO and Mg^{2+} species, respectively. In addition, the Sn 3d region, provided in Fig. 2(e), also shows three peaks, here at binding energies of 485.4 eV, 486.1 eV, and 486.6 eV, attributed to Sn, SnO and SnO_2, respectively.[33] The generation of magnesium and tin oxides is due to the inevitable oxidation of BiSn@Mg during the XPS test. Finally, the Cl 2p region, provided in Fig. 2(f), shows peaks located at 198.5 eV and 199.9 eV, assigned to the $2p_{3/2}$ and $2p_{1/2}$ of Cl^-,[35] and attributed to the residues resulting from reactions of Mg with $BiCl_3/SnCl_2$. Consequently, the artificial interface on the Mg surface can be inferred to be mainly composed of metallic Bi and Sn.

Charge–discharge curves of the BiSn@Mg and Mg anodes acquired under same conditions in Fig. 3(a) and (b) indicate a nucleation overpotential of Mg of about 0.098 V on the BiSn@Mg anode, and of 3.21 V on the Mg anode. Meanwhile, it can also be found that the overpotential difference of the Mg//SS runs to 5.06 V, which is almost 24.1 times higher than that of BiSn@Mg//SS (0.21 V). The significant reduction of nucleation and plateau overpotential on BiSn@Mg anode originates from the formation of artificial interface.[32] Fig. S8 and S10 (ESI†) show that BiSn@Mg//BiSn@Mg has the lowest activation energy and interfacial resistance, due to the synergy of Bi and Sn, thereby enhancing Mg^{2+} adsorption and diffusion.[33] Additionally, the results of a cycling stability test on BiSn@Mg//BiSn@Mg, provided in Fig. 3(c), indicate an enduring and stable cycling performance, attributed to the formation of the artificial interface. After 20 charging–discharging cycles, the overpotential of BiSn@Mg//BiSn@Mg is approximately 0.18 V, much lower than that of Mg//Mg (2.0 V). It still remains at about 0.2 V after 4000 h of charge–discharge at 0.01 mA cm^{-2} with a coulombic efficiency of 99%, as shown in Fig. S6(a) (ESI†). However, the results displayed in Fig. S6(c) (ESI†) show that under the same conditions, Sn@Mg//Sn@Mg and Bi@Mg//Bi@Mg can operate continuously for 100 and 500 h, while the Mg//Mg device only stably runs for 60 h. Similarly, the results in Fig. S6(d) (ESI†) indicate that the overpotentials of Sn@Mg//Sn@Mg and Bi@Mg//Bi@Mg separately are 0.5 V and 0.6 V, much higher than that of BiSn@Mg//BiSn@Mg. From rate capability data acquired for BiSn@Mg//BiSn@Mg, shown in Fig. 3(d), its overpotential can be found to increase gradually from 0.15 to 0.3 V as the current density is increased from 0.01 to 0.2 mA cm^{-2}. When the current density reverts to 0.01 mA cm^{-2}, the cell overpotential also drops back to 0.15 V. These results imply a good rate capability for BiSn@Mg//BiSn@Mg. However, rate capability data acquired for Mg//Mg and displayed in Fig. 3(e) show that its overpotential remains at almost 2.0 V under different current densities. These results sufficiently clearly demonstrate an improvement in performance resulting from fabricating the artificial interface on the Mg anode. Similarly, the data displayed in Fig. S6(e) and (f) (ESI†) show that both Sn@Mg//Sn@Mg and Bi@Mg//Bi@Mg experience short-circuiting when the current density is increased to 0.05 mA cm^{-2}. In addition, the data in Fig. S9 (ESI†) also indicate that the ratio of the amount of Bi^{3+} to that of Sn^{2+} and the reaction time significantly affect the performances of BiSn@Mg. The overpotential of BiSn@Mg//BiSn@Mg is lowest when this ratio is 1 : 1. Moreover, under this optimal ratio, the overpotential decreases first and then after 14 minutes increases with the increasing reaction time, leading us to choose 14 minutes as the optimal reaction time in this work.

The CV curves acquired of BiSn@Mg//Mo and provided in Fig. 4(a) show a pair of redox peaks at 0.70 V and −0.75 V, which correspond to the stripping and plating of Mg. However, no redox peaks appear on the CV curves of Mg//Mo, displayed in Fig. 4(b). These results imply that fabricating an artificial interface is conducive to enhancing Mg plating and stripping, and remarkably improving electrochemical behaviours. EIS data acquired before the charge–discharge and displayed in Fig. 4(c) and (d) and Table S1 (ESI†) demonstrate that the reaction resistance of BiSn@Mg//BiSn@Mg is 3.7 kΩ, much

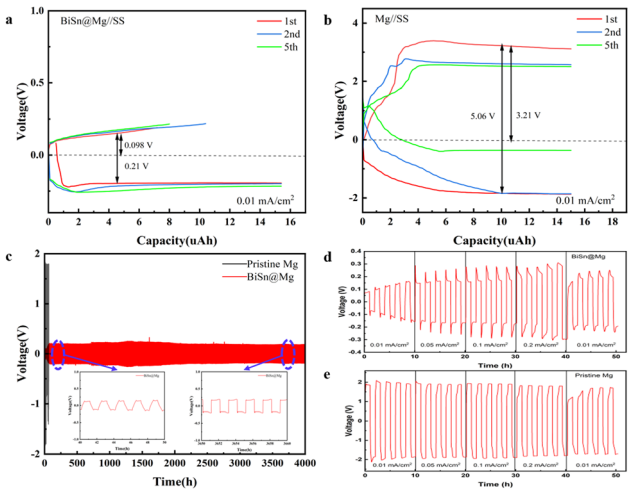

Fig. 3 (a) and (b) Charge–discharge curves of (a) BiSn@Mg//SS and (b) Mg//SS. (c) Cycling stability levels of indicated cells at 0.01 mA cm^{-2} (with enlarged views of 40–50 and 3650–3660 h in the inset). (d) and (e) Rate capability levels of the (d) BiSn@Mg//BiSn@Mg and (e) Mg//Mg cells.

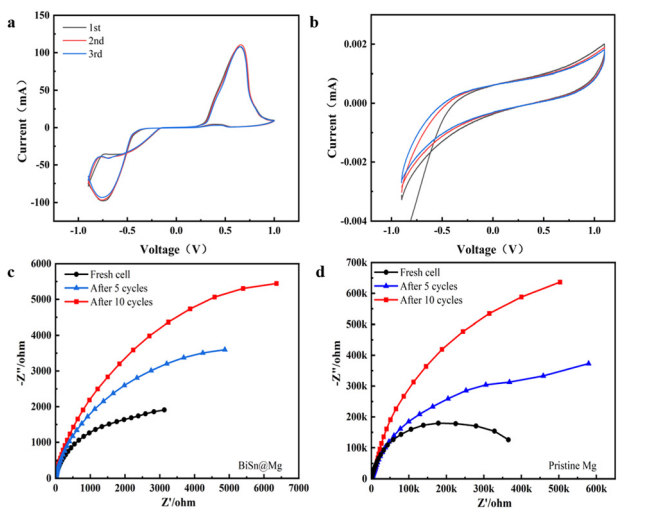

Fig. 4 (a) and (b) CV curves of (a) BiSn@Mg//Mo and (b) Mg//Mo in 0.5 M $Mg(TFSI)_2$/DME at 10 mV s^{-1}. (c) and (d) EIS of (c) BiSn@Mg//BiSn@Mg and (d) Mg//Mg under indicated cycling states.

lower than that of Mg//Mg (489.1 kΩ). This difference can be attributed to the formation of the artificial interface, and its enhancement of the diffusion kinetics of Mg^{2+}. Although all the cells tested show a tendency of increasing reaction resistance during the course of charge–discharge, the value of BiSn@Mg//BiSn@Mg is always much lower than that of Mg//Mg, suggesting that the rise of reaction impedance is inhibited by the artificial interface, thereby improving cycling stability.

The CV curves acquired of BiSn@Mg//Mo_6S_8 and displayed in Fig. S12(a) (ESI†) show redox signals located at about 0.6 V and −0.6 V, respectively, and the positions and current density remaining stable in the subsequent cycles, suggesting good reaction kinetics and stability. However, there are no obvious redox signals in the CV curves acquired for Mg//Mo_6S_8 and shown in Fig. S12(b) (ESI†). This result stems from the difficulty of plating and stripping on the Mg anode. The results in Fig. S12(c) and (e) (ESI†) show that BiSn@Mg//Mo_6S_8 displays a charge–discharge plateau and a discharge specific capacity of 49 mA h g^{-1} with a coulombic efficiency of 87.4% during the first cycle. Also, the discharge specific capacity can still reach 39 mA h g^{-1} after 20 cycles. However, Mg//Mo_6S_8 shows a much lower specific capacity and coulombic efficiency; see Fig. S12(d) and (f) (ESI†).

Herein, an artificial interface consisting of metallic Bi and Sn has been successfully fabricated on an Mg anode by performing a replacement reaction, yielding excellent electrochemical performances. The nucleation and deposition overpotentials for the BiSn@Mg anode are much lower than those for the Mg anode under the same conditions. BiSn@Mg//BiSn@Mg generates an overpotential of only 0.2 V at 0.01 mA cm^{-2} and can run stably for 4000 h with good rate capability and coulombic efficiency. However, Mg//Mg does not work normally after 60 h, and its overpotential is about 2.0 V. Moreover, BiSn@Mg//Mo_6S_8 can provide an initial discharge specific capacity of 49 mA h g^{-1}. These excellent performance measures are attributable to the formation of the artificial interface on the Mg anode surface, which lowers the energy barrier of Mg^{2+} adsorption and diffusion as well as lowering the reaction impedance, thus improving the affinity of Mg to the anode-electrolyte interface and improving electrode reaction kinetics. These research results contribute to the advancement of modification methodologies for Mg anode surfaces to facilitate the development of high-performance RMBs.

This work is supported by the National Key Research and Development Program of China (No. 2023YFB3809500 and No. 2021YFB4000300). We would like to thank the Testing Center of Chongqing University for their help in the characterization of material properties.

Conflicts of interest

There are no conflicts to declare.

Data availability

The data supporting this article have been included as part of the ESI.†

Notes and references

1 J. M. Tarascon and M. Armand, *Nature*, 2001, **414**, 359–367.
2 P. G. Bruce, S. A. Freunberger, L. J. Hardwick and J.-M. Tarascon, *Nat. Mater.*, 2012, **11**, 19–29.
3 P. G. Bruce, B. Scrosati and J.-M. Tarascon, *Angew. Chem., Int. Ed.*, 2008, **47**, 2930–2946.
4 G. Zhou, F. Li and H.-M. Cheng, *Energy Environ. Sci.*, 2014, **7**, 1307–1338.
5 D. Li, C. Zhu, M. Zhang, Y. Wang, Z. Kang, Y. Liu, J. Liu, J. Liu and H. Xie, *Chem. Eng. J.*, 2021, **408**, 127335.
6 P. Canepa, G. Sai Gautam, D. C. Hannah, R. Malik, M. Liu, K. G. Gallagher, K. A. Persson and G. Ceder, *Chem. Rev.*, 2017, **117**, 4287–4341.
7 C. Wei, L. Tan, Y. Zhang, Z. Wang, J. Feng and Y. Qian, *Energy Storage Mater.*, 2022, **52**, 299–319.
8 S. Li, M. Jiang, Y. Xie, H. Xu, J. Jia and J. Li, *Adv. Mater.*, 2018, **30**, 1706375.
9 C. Cui, R. Zhang, C. Fu, R. Xiao, R. Li, Y. Ma, J. Wang, Y. Gao, G. Yin and P. Zuo, *Chem. Eng. J.*, 2022, **433**, 133570.
10 N. Harpak, G. Davidi and F. Patolsky, *Chem. Eng. J.*, 2022, **429**, 132077.
11 X. Li, T. Gao, F. Han, Z. Ma, X. Fan, S. Hou, N. Eidson, W. Li and C. Wang, *Adv. Energy Mater.*, 2018, **8**, 1701728.
12 S.-B. Son, T. Gao, S. P. Harvey, K. X. Steirer, A. Stokes, A. Norman, C. Wang, A. Cresce, K. Xu and C. Ban, *Nat. Chem.*, 2018, **10**, 532–539.
13 I. Shterenberg, M. Salama, H. D. Yoo, Y. Gofer, J.-B. Park, Y.-K. Sun and D. Aurbach, *J. Electrochem.*, 2015, **162**, A7118.
14 H. D. Yoo, S.-D. Han, I. L. Bolotin, G. M. Nolis, R. D. Bayliss, A. K. Burrell, J. T. Vaughey and J. Cabana, *Langmuir*, 2017, **33**, 9398–9406.
15 O. Tutusaus, R. Mohtadi, N. Singh, T. S. Arthur and F. Mizuno, *ACS Energy Lett.*, 2017, **2**, 224–229.
16 J. Zhang, J. Liu, M. Wang, Z. Zhang, Z. Zhou, X. Chen, A. Du, S. Dong, Z. Li, G. Li and G. Cui, *Energy Environ. Sci.*, 2023, **16**, 1111–1124.
17 Y. Liu, W. Zhao, Z. Pan, Z. Fan, M. Zhang, X. Zhao, J. Chen and X. Yang, *Angew. Chem., Int. Ed.*, 2023, **62**, e202302617.
18 Y. Zhang, H. Geng, W. Wei, J. Ma, L. Chen and C. C. Li, *Energy Storage Mater.*, 2019, **20**, 118–138.
19 M. Farrag, H. S. Refai and E. Sheha, *J. Solid State Electrochem.*, 2023, **27**, 379–389.
20 A. R. Jeon, S. Jeon, G. Lim, J. Jang, W. J. No, S. H. Oh, J. Hong, S.-H. Yu and M. Lee, *ACS Nano*, 2023, **17**, 8980–8991.
21 C. Pechberty, A. Hagopian, J.-B. Ledeuil, D. Foix, J. Allouche, J.-N. Chotard, O. Lužanin, J. Bitenc, R. Dominko, R. Dedryvère, J.-S. Filhol, L. Stievano and R. Berthelot, *J. Mater. Chem. A*, 2022, **10**, 12104–12113.
22 Y. Wang, E. Sahadeo and S. B. Lee, *ACS Appl. Energy Mater.*, 2022, **5**, 2613–2620.
23 X. Li, Q. Liu, X. Wang, J. Liu, M. Cheng, J. Hu, T. Wei, W. Li, Y. Ling, B. Chen, Z. Pan, W. Ma, B. Liu, Z. Wu, J. Liu and Y. Zhang, *Electrochim. Acta*, 2022, **414**, 140213.
24 M. Ulusel, O. Dinçer, O. Şahin and S. Çınar-Aygün, *ACS Appl. Mater. Interfaces*, 2023, **15**, 51309–51318.
25 J. Zhang, X. Guan, R. Lv, D. Wang, P. Liu and J. Luo, *Energy Storage Mater.*, 2020, **26**, 408–413.
26 R. Lv, X. Guan, J. Zhang, Y. Xia and J. Luo, *Natl. Sci. Rev.*, 2020, **7**, 333–341.
27 C. Li, D. Liu, M. Huang, W. Huang, Y. Li and J. Feng, *Food Hydrocolloids*, 2022, **127**, 107552.
28 X. Wang, Y. Pan, X. Wang, Y. Guo, C. Ni, J. Wu and C. Hao, *Ind. Crops Prod.*, 2022, **189**, 115863.
29 Y. Chen, X. Shen, J. Wang, Y. Zhang, Y. Hao, L. Tong, G. Huang, Q. Li, X. Zhou, B. Qu and F. Pan, *ACS Energy Lett.*, 2024, **9**, 5616–5626.
30 Q. Wu, Y. Zhong, R. Chen, G. Ling, X. Wang, Y. Shen and C. Hao, *Ind. Crops Prod.*, 2024, **222**, 119676.
31 C. Wu, L. Xue, R. Xu, J. Fan, T. Chen, W. Tang, L. Cui, A. Wang, S. X. Dou and C. Peng, *Mater. Today Energy*, 2024, **40**, 101485.
32 H. Chu, N. Yuan, K. Zhang, Z. Zhou, K. Chao, G. Li and Z. Zhang, *Appl. Surf. Sci.*, 2024, **643**, 158636.
33 H. Chu, Z. Zhang, Z. Song, A. Du, S. Dong, G. Li and G. Cui, *Chem. Commun.*, 2021, **57**, 9430–9433.
34 A. Dutta, I. Zelocualtecatl Montiel, K. Kiran, A. Rieder, V. Grozovski, L. Gut and P. Broekmann, *ACS Catal.*, 2021, **11**, 4988–5003.
35 T. Gao, S. Hou, K. Huynh, F. Wang, N. Eidson, X. Fan, F. Han, C. Luo, M. Mao, X. Li and C. Wang, *ACS Appl. Mater. Interfaces*, 2018, **10**, 14767–14776.

